2004-07-20

3D analysis of hybrid photonic crystal/ conventional waveguide 90° bend

J. Cai

S. Kim

See next page for additional authors

Original Publication Citation
J. Cai, G. P. Nordin, S. Kim, and J. Jiang,"3D analysis of hybrid photonic crystal/conventional waveguide 9° bend," Appl. Opt. 43(21), pp. 4244-4249 (24)

Three-dimensional analysis of a hybrid photonic crystal–conventional waveguide 90° bend

Jingbo Cai, Gregory P. Nordin, Seunghyun Kim, and Jianhua Jiang

We present a three-dimensional (3D) analysis of a hybrid photonic crystal–conventional waveguide 90° bend proposed previously [Opt. Express **10,** 1334 (2002)] as an ultracompact component for large-scale planar lightwave circuit integration. Both rigorous 3D finite-difference time-domain modeling and a simple perfect mirror model analysis were carried out for different Si post heights in the photonic crystal region. Results show that the bend efficiency increases rapidly with Si post height. For a post height of 6.5 μm, this structure yields a bend efficiency of 97.3% at a wavelength of 1.55 μm for 90° bends in 2 μm × 2 μm square channel conventional waveguides with a refractive index contrast of 3.55%, which is very close to the bend efficiency of 98.2% for the corresponding two-dimensional problem. Our 3D analysis permits the examination of issues such as out-of-plane scattering loss and the effects of finite Si post height that are not considered in two dimensions. © 2004 Optical Society of America

OCIS codes: 130.0130, 130.1750, 130.2790, 130.3120, 250.5300.

1. Introduction

Photonic crystal (PhC) structures have been extensively studied recently, partly because of their potential for use in ultracompact planar light-wave circuits (PLCs). Much of the research reported in the literature has focused on creating fundamental elements of PLCs such as waveguides, bends, splitters, and resonators by introducing suitable defect features in a two-dimensional (2D) PhC slab. These approaches involve difficult issues such as scattering loss,[1–3] the relationship of defect waveguide modes to the light line,[4–6] single-mode versus multimode waveguide operation,[4,7,8] and flatness of the dispersion relation of the fundamental guided mode.[9] In a previous paper[10] we suggested the hybrid integration of conventional waveguides (CWGs) and PhC structures to dramatically reduce the sizes of PLCs and yet keep the appealing properties of CWGs. In our analysis we considered two spatial dimensions. In this paper we present a full three-dimensional (3D) analysis of a hybrid PhC–CWG 90° bend, using 3D finite-difference time-domain (FDTD) simulation to examine issues such as out-of-plane scattering loss and modal coupling.

The geometry of the 90° bend shown in Fig. 1 consists of two components: a 90° bent channel waveguide and a small PhC region composed of Si posts that straddle the waveguide symmetrically in the vertical dimension and are arranged in a square array at the outside corner of the waveguide bend. The Si posts have a radius of 86.8 nm, and the PhC lattice constant is 380 nm. The waveguide core has a 2 μm by 2 μm cross section with a refractive index of 1.519, which gives the same 2D effective index of 1.5 as used in our previous 2D analysis.[10] The waveguide cladding and Si posts also have the same refractive indices, of 1.465 and 3.481, respectively. The bend efficiency, which is the ratio of the power in the excited guided mode in the output waveguide to the power in the sourcing guided mode in the input waveguide, is studied as a function of the post height in the PhC region. Our results show that, as the post height is increased, out-of-plane scattering loss is quickly reduced and performance comparable to 2D simulation is obtained.

To reduce computation time and fit our data into RAM memory resources, we parallelized our 3D FDTD code, using the MPI (message passing interface) Library.[11,12] The computational domain was divided into slabs along the input waveguide direction, and it is run on a 32-node PC (2-GHz CPU, 1-Gbyte RAM) Linux cluster. As a comparison, we also developed a simple intuitive model that treats

The authors are with the Nano and Micro Devices Center, University of Alabama in Huntsville, Huntsville, Alabama 35899. G. P. Nordin's e-mail address is nordin@ece.uah.edu.

Received 2 September 2003; revised manuscript received 17 March 2004; accepted 28 April 2004.

0003-6935/04/214244-06$15.00/0

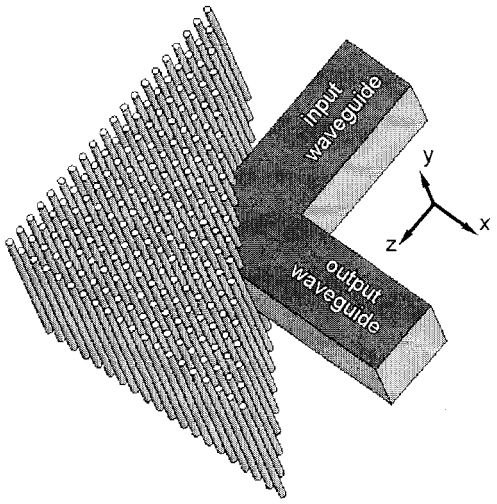

Fig. 1. Hybrid PhC–CWG 90° bend. See text for details.

the PhC region as a perfect mirror and assumes that the portion of the input waveguide mode incident upon it is completely reflected toward the output waveguide direction. Then bend efficiencies are calculated and compared with those generated on the basis of FDTD simulation data. We have found that this model adequately explains the behavior calculated with 3D FDTD analysis.

In Section 2 we describe sourcing the waveguide guided mode needed for our 3D FDTD analysis. In Section 3 the fields and the Poynting vector magnitude in selected planes for 90° bends with 5- and 3-μm Si posts are studied and compared as an aid in understanding the effects of post height on the interaction of light with the bend. Section 4 shows the dependence of bend efficiency on post height based on FDTD analysis as a function of post height. In addition, an analysis based on a perfect-mirror model of the PhC region is given in that section, and its results are compared with those from 3D FDTD analysis.

2. Sourcing of the Guided Mode

A total-field–reflected-field modal formulation[13] of the FDTD algorithm was used to launch a modal wave into the input waveguide. For a rectangular channel waveguide, transverse field distributions and the propagation constant of a mode can be calculated approximately by Marcatili's method.[14] To improve the accuracy of the launched mode's transverse field distribution, we carried out a mode bootstrapping[13] FDTD simulation of a straight waveguide three consecutive times in a FDTD computational volume of 7 μm by 7 μm by 6 μm along the x, y, and z axes, respectively, with a 15-nm Yee cell. The mode profile bootstrapped from the previous run was then used for the next bootstrapping run. To maintain the same field polarization as that of the TM polarization (electric field orientation parallel to the PhC posts) used in our 2D simulation, we used the $E_{11}{}^{y}$ mode of the waveguide by Marcatili's method for light with a free-space wavelength of 1.55 μm to launch the mode in the waveguide in the first bootstrapping run. Each bootstrapping tended to improve the mode profile to some extent by shedding power in leaky modes. The field profiles bootstrapped from the third run were used later to launch a sourcing mode in the input waveguide of the FDTD model of the PhC–CWG 90° bend. Thus a total waveguide length of ~15 μm was used to bootstrap the sourcing mode from the approximate mode of Marcatili. Figures 2(a) and 2(b) show the normalized E_y amplitude and the normalized Poynting vector z component of the sourcing mode. They serve as a reference for interpretation of the fields and Poynting vector components plotted in Figs. 3 and 4. The squares in the figures represent cross sections of the channel waveguide.

We also used the 3D waveguide mode solver package OEDCAD[15] to calculate the mode profile of the bootstrapping waveguide. Mode profile fields E_y from OEDCAD and our bootstrapping procedure along the x and y axes are plotted in Figs. 2(c) and 2(d), respectively. There is reasonable agreement between the two methods even though the equivalent total length of the bootstrapping waveguide was just 15 μm. We are now evaluating the direct use of the output of a mode solver such as OEDCAD as a source for a 3D FDTD. When it is completed, our study will permit us to source modes supported by more-complex waveguide geometries. For purposes of this paper we used the bootstrapped mode described above.

3. Modeling Results for 5- and 3-μm Post Heights

We modeled the hybrid PhC–CWG 90° bend in a FDTD computational volume of 11.95 μm by 7.0 μm by 10.35 μm along the x, y, and z dimensions, respectively. This computational volume was terminated by a 10-cell PML Berenger absorbing boundary.[13] A cubic Yee cell of 15 nm on a side was used. The origin of the coordinate system was positioned at the center of the FDTD computational volume. The bootstrapped modal source, which is plotted in Fig. 2, was used to excite the input waveguide of the structure. After FDTD time marching reached steady state, field information in four planes was extracted by Fourier transformation of field values in these planes over one period of the light wave. These four planes were chosen to be (1) the $y = 0$ μm plane, which is the vertical symmetry plane of the entire structure; (2) the $y = 3.3$ μm plane, which is 2.3 μm above the top surface of the channel waveguide and 0.05 μm above the tip of 6.5 μm Si posts (the maximum of Si post height studied in this paper); (3) the $z = 5.1$ μm plane, which is just beyond the PhC region and normal to the input waveguide direction; and (4) the $x = 5.0$ μm plane, which is normal to the output waveguide and 6.0 μm from the inside corner of the waveguide.

Values of the E_y field amplitude in Figs. 2–4 were normalized with respect to the maximum amplitude of the E_y field of the modal source. Similarly, values of the y component of the Poynting vector were nor-

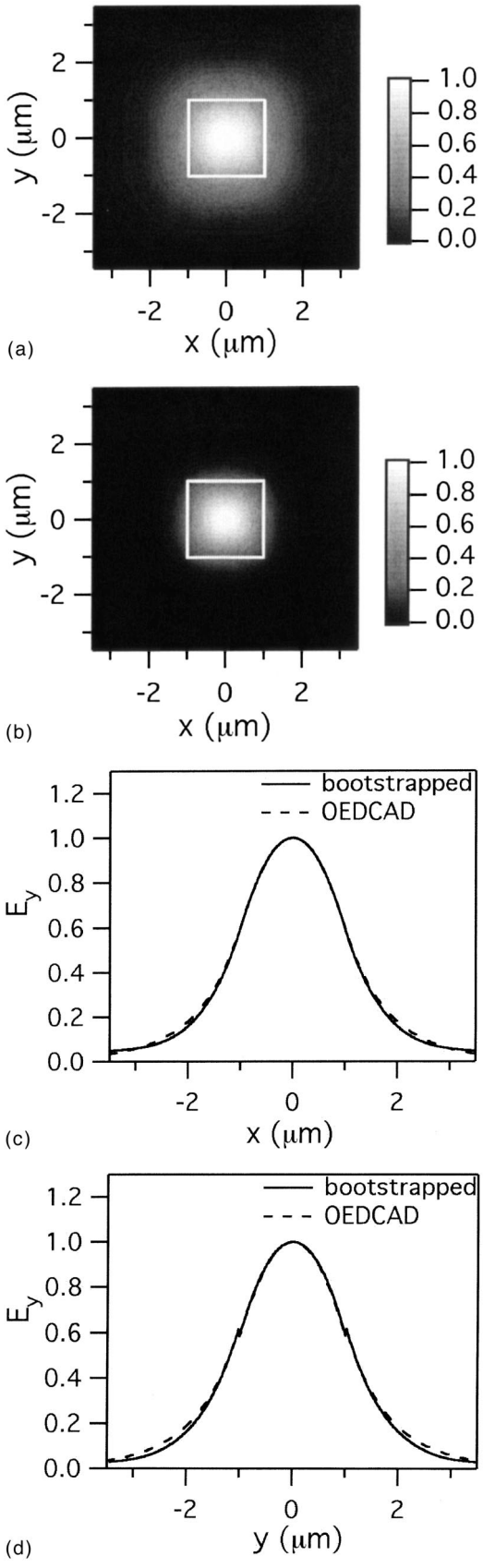

Fig. 2. Cross section of a waveguide with (a) E_y amplitude and (b) Poynting vector z components of the sourcing mode. (c), (d) Comparisons in the x and y directions, respectively, of mode profiles obtained by bootstrapping and the mode solver package OEDCAD.

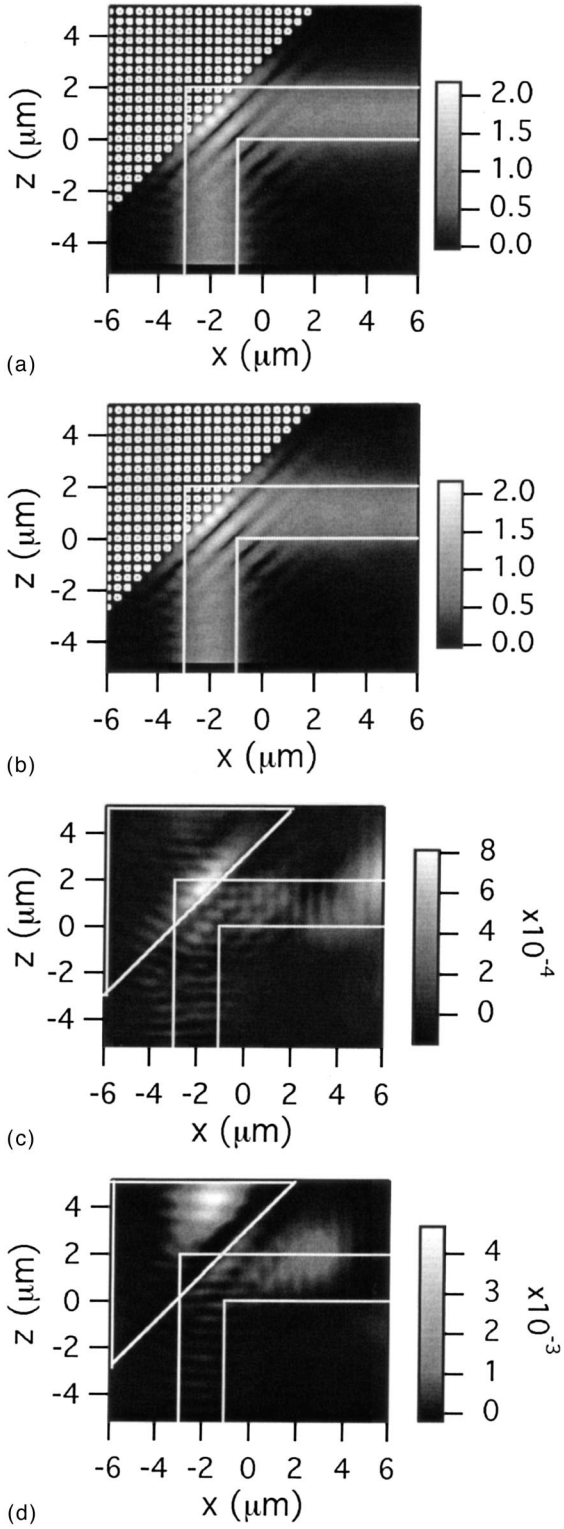

Fig. 3. Case 1 (5.0-μm post height) and case 2 (3.0-μm post height). (a) E_y amplitude, $y = 0$ μm, case 1. (b) E_y amplitude, $y = 0$ μm, case 2. (c) y component of Poynting vector, $y = 3.3$ μm, case 1. (d) y component of Poynting vector, $y = 3.3$ μm, case 2.

malized with respect to the maximum magnitude of the Poynting vector of the modal source.

The E_y amplitude in the $y = 0$ plane for both 5.0- and 3.0-μm Si post heights is plotted in Figs. 3(a) and

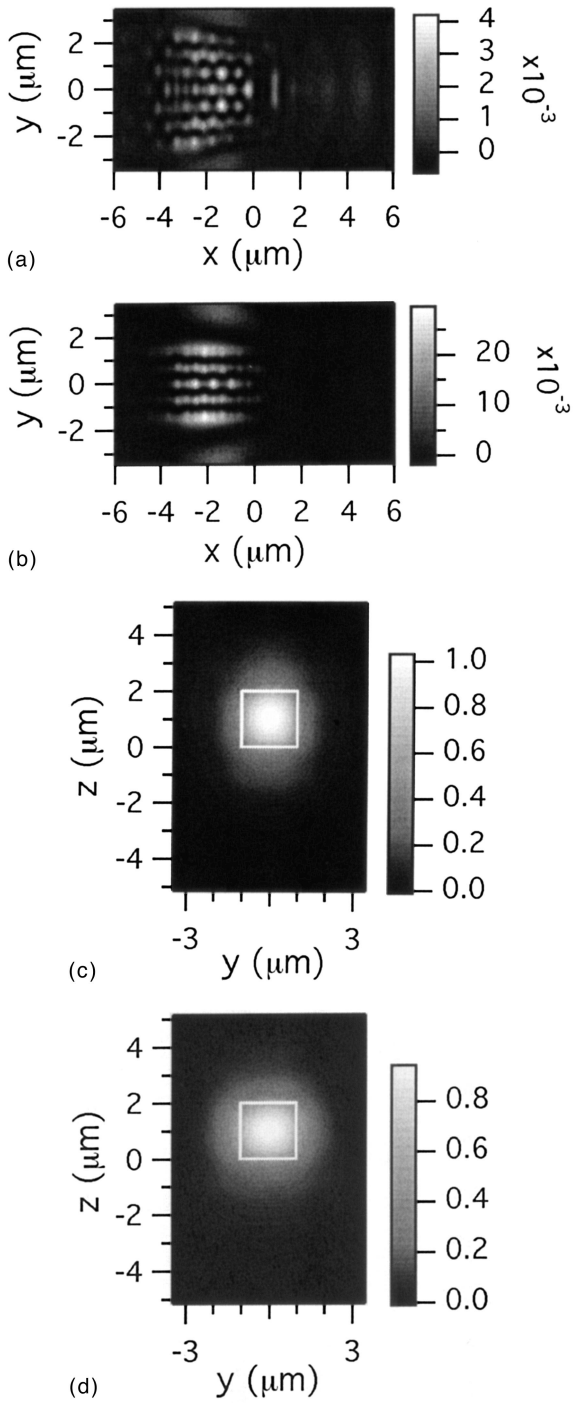

Fig. 4. Case 1 (5.0-μm post height), case 2 (3.0-μm post height). (a) z component of Poynting vector, $z = 5.1$ μm, case 1. (b) z component of Poynting vector, $z = 5.1$ μm, case 2. (c) E_y amplitude, $x = 5.0$ μm, case 1. (d) E_y amplitude, $x = 5.0$ μm, case 2.

3(b), which can be compared directly with the 2D simulation results of our previous paper.[10] The field patterns for the two heights in the $y = 0$ plane are very similar [Figs. 3(a) and 3(b)]. They both show, just like the 2D modeling results in our previous paper,[10] little penetration of the field into the PhC region, a neatly reflected field pattern, and the expected straight interference fringes at the bend corner.

To evaluate the out-of-plane scattering, we plotted the y component of the Poynting vector in the $y = 3.3$ μm plane for both cases in Figs. 3(c) and 3(d). The Poynting vector y component for the 5-μm post height is significantly smaller than that for the 3-μm post height (note the different scales used in the color maps of the figures). These results demonstrate a much smaller out-of-plane scattering for the 5-μm post length. In addition, the patterns of out-of-plane scattering were different for the two cases. For the 5-μm post there is a spot of strong out-of-plane radiation directly above the interface of the PhC region with the conventional waveguide region. For the 3-μm post there is a region of strong out-of-plane radiation along the extension of the input waveguide and above the PhC region near the boundary of the computational volume.

The interpretation of these radiation patterns is straightforward. For the 5-μm post the sourcing guided mode, as it propagates down the input waveguide, encounters a PhC region that it cannot enter, and a small fraction of it is scattered either up or down along the front face of the PhC region as out-of-plane radiation. For the 3-μm post the same sourcing guided mode encounters a PhC region, which is smaller in the y dimension, and consequently a portion of its mode tail propagates straight over the top of the PhC region. This portion of the mode tail breaks away from the waveguide and radiates as out-of-plane scattering some distance along the direction of the input waveguide.

Another noteworthy point illustrated in Figs. 3(c) and 3(d) is that the region directly above the output waveguide has an obviously stronger out-of-plane component of Poynting vector than the region directly above the input waveguide does. This shows that the light deflected into the output waveguide is not a settled guided mode yet because some portion of it escapes the waveguide as out-of-plane radiation.

Figures 4(a) and 4(b) show the z component of the Poynting vector in the $z = 5.1$ μm plane for post heights of 5 and 3 μm, respectively. These fringe patterns are due to the interference between the two unobstructed portions of the incident mode passing above and beneath the PhC region that are deflected into the region behind the PhC by diffraction at the rear PhC edges. Note the constructive fringe at the center of Figs. 4(a) and 4(b), which is comparable to the bright Poisson spot formed behind an opaque object in diffraction phenomena. The maximum value in Fig. 4(b) is larger than in Fig. 4(a) because the individual interfering beams are stronger for the 3-μm posts, for which there is less obstruction of the incident mode by the PhC.

Figures 4(c) and 4(d) show the E_y amplitude at the $x = 5$ μm plane normal to the output waveguide for post heights of 5 and 3 μm, respectively. The field profiles in Figs. 4(c) and 4(d) vary from that of the sourcing mode shown in Fig. 2(a) because of the existence of radiation modes, as can be seen from Figs. 3(c) and 3(d).

The actual power of the guided mode excited in the

Table 1. Efficiencies for Several Post Heights

Post Height (μm)	Parameter			
	η_{corner}	η_{bend}	η_{corner}^{m}	η_{bend}^{m}
2	0.790	0.658	0.811	0.653
2.5	0.872	0.779	0.893	0.791
3	0.940	0.886	0.941	0.882
4	0.977	0.951	0.983	0.964
5	0.985	0.966	0.996	0.991
6.5	0.986	0.973	1.000	0.999
Infinity[a]	0.987	0.982		

[a]Calculated from 2D FDTD analysis.

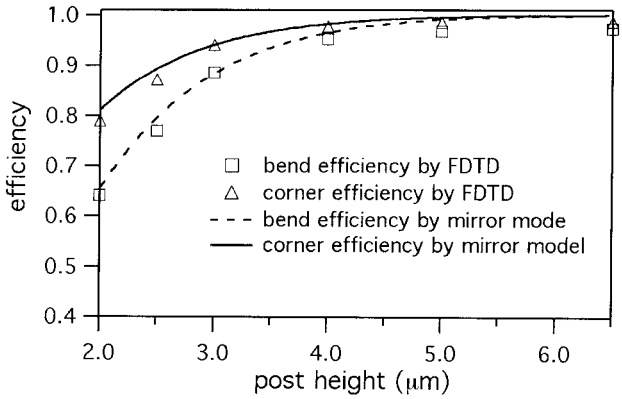

Fig. 5. Efficiency as a function of post height.

output waveguide can be calculated through an overlap integral[16,17] between the field distribution at the $x = 5$ μm plane and the guided mode's field profile. We define the corner efficiency η_{corner} as the ratio of the optical power, integrated over a 7 μm by 7 μm rectangular area centered about the output waveguide and in the $x = 5$ μm plane, to the optical power of the input sourcing mode over a 7 μm by 7 μm rectangular area. Bend efficiency η_{bend}, which is the ratio of the power in the guided mode excited in the output waveguide to the power of the sourcing mode, is calculated from

$$\eta_{bend} = \eta_{corner} \times \eta_c, \tag{1}$$

$$\eta_c = \frac{\left| \iint (\vec{E}_p^{\,*} \times \vec{H}_q + \vec{E}_q \times \vec{H}_p^{\,*}) \mathrm{d}\vec{s} \right|^2}{\left| \iint (\vec{E}_p^{\,*} \times \vec{H}_p + \vec{E}_p \times \vec{H}_p^{\,*}) \mathrm{d}\vec{s} \right| \left| \iint (\vec{E}_q^{\,*} \times \vec{H}_q + \vec{E}_q \times \vec{H}_q^{\,*}) \mathrm{d}\vec{s} \right|}, \tag{2}$$

where η_c is the butt coupling coefficient.[14] For our case, $\mathbf{E}_p$ and $\mathbf{H}_p$ are the electric and magnetic field profiles at the $x = 5$ μm plane and $\mathbf{E}_q$ and $\mathbf{H}_q$ are the modal profiles supported by the output waveguide, which is the same as that of the sourcing mode. From our FDTD simulation data we found that the 5-μm posts have $\eta_{corner} = 98.5\%$, butt coupling efficiency $\eta_c = 98.1\%$, and $\eta_{bend} = 96.6\%$, whereas the 3-μm posts have $\eta_{corner} = 94.0\%$, $\eta_c = 94.2\%$, and $\eta_{bend} = 88.6\%$. For comparison, the 2D 90° bend discussed in our previous paper[10] had 98.7% for η_{corner}, 99.5% for η_c, and 98.2% for η_{bend}. With a 6.5-μm post height we got 98.6% for η_{corner}, 98.7% for η_c, and 97.3% for η_{bend}, which are very close to the 2D results.

4. Effect of Post Height

To study the dependence of η_{bend} and η_{corner} on the height of the Si posts, we simulated 2-, 2.5-, 3-, 4-, 5-, and 6.5-μm posts. The results are listed in Table 1 and plotted as a function of post height in Fig. 5. Clearly, as the post height increases, the fraction of the input mode that is reflected (η_{corner}) also increases. Likewise, the fraction of the mode that is reflected more closely matches the mode supported by the output waveguide, so η_{bend} increases even faster.

We can draw an analogy between the functionality of the PhC region with that of a perfect mirror.[10] In the perfect-mirror model, the sourcing guided mode is assumed to be clipped by the boundary face of the PhC region just as an incident wave front is clipped by a limited height mirror, and the portion intercepted is considered to be reflected completely toward the output waveguide, as illustrated in Fig. 6. Let us now define mirror-model corner efficiency η_{corner}^{m}, mirror-model butt-coupling efficiency η_c^{m}, and mirror-model bend efficiency η_{bend}^{m} in the same way as we have done for corner efficiency, butt-coupling efficiency, and bend efficiency. The calculated η_{corner}^{m} and η_{bend}^{m} for 2-, 2.5-, 3-, 4-, 5-, and 6.5-μm posts are also listed in Table 1 and plotted in Fig. 5 as a function of post height. Note the excellent agreement with the 3D FDTD results.

Both the perfect-mirror model and 3D FDTD analysis predict that the bend efficiency and the corner efficiency will increase significantly as the Si post height increases from 2.0 to ~4 μm. Beyond this, both efficiencies vary slightly as the Si post height is changed because only a small percentage of the guided mode energy is associated with the tail outside the 4.0-μm central range of the mode. Hence, increasing post height has less effect on both corner and bend efficiencies than it does for smaller post heights. The perfect-mirror model shows both the corner and bend efficiencies converge to 1 as post height is increased. However, 3D FDTD analysis

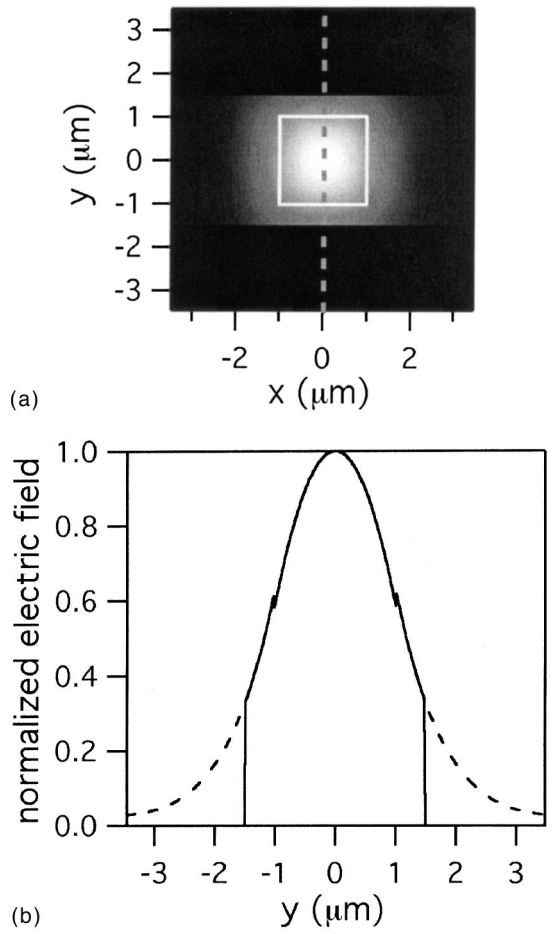

Fig. 6. Clipping of a mode by a perfect mirror. (a) Mode clipped by a perfect mirror 3 μm tall in the *y* dimension. (b) Clipped field profile along the dotted line in (a). Dashed curve, clipped part of the mode.

shows that both efficiencies are high but are always slightly less than 1 at large post heights. This is so because the perfect-mirror model considers only vertical clipping of the input mode, whereas 3D FDTD analysis takes into account all other scattering losses.

5. Summary

Our 3D FDTD analysis clearly shows the effects of finite Si post height in the PhC region of a hybrid PhC–CWG 90° bend. The taller the posts, the greater the intersection of the PhC region with the vertical extent of the waveguide mode and hence the greater the bend efficiency. The 3D FDTD results agree well with a perfect-mirror model based on this phenomenon. Moreover, for large Si post heights, 3D FDTD results also show good agreement with our previously reported 2D results.[10]

This study was supported in part by Defense Advanced Research Projects Agency grant N66001-01-8938 and National Science Foundation grant EPS-0091853.

References

1. H. Benisty, D. Labilloy, C. Weisbuch, C. J. M. Smith, T. F. Krauss, D. Cassagne, A. Beraud, and C. Jouanin, "Radiation losses of waveguide-based two-dimensional photonic crystals: positive role of the substrate," Appl. Phys. Lett. **76,** 532–534 (2000).
2. W. Bogaerts, P. Bienstman, D. Taillaert, R. Baets, and D. D. Zutter, "Out-of-plane scattering in photonic crystal slabs," IEEE Photon. Technol. Lett. **13,** 565–567 (2001).
3. P. Lalanne and H. Benistry, "Out-of-plane losses of two-dimensional photonic crystals waveguides: electromagnetic analysis," J. Appl. Phys. **89,** 1512–1514 (2001).
4. A. Chutinan and S. Noda, "Waveguides and waveguide bends in two-dimensional photonic crystal slabs," Phys. Rev. B **62,** 4488–4492 (2000).
5. P. Lalanne, "Electromagnetic analysis of photonic crystal waveguides operating above the light cone," IEEE J. Quantum Electron. **38,** 800–804 (2002).
6. M. Tokushima and H. Yamada, "Light propagation in a photonic-crystal-slab line-defect waveguide," IEEE J. Quantum Electron. **38,** 753–759 (2002).
7. A. Adibi, Y. Xu, R. K. Lee, A. Yariv, and A. Scherer, "Properties of the slab modes in photonic crystal optical waveguides," J. Lightwave Technol. **18,** 1554–1564 (2000).
8. M. Notomi, A. Shinya, K. Yamada, J. Takahashi, C. Takahashi, and I. Yokohama, "Structural tuning of guiding modes of line-defect waveguides of silicon-on-insulator photonic crystal slabs," IEEE J. Quantum Electron. **38,** 736–742 (2002).
9. S. Olivier, H. Benisty, C. Weisbuch, C. J. M. Smith, T. F. Krauss, R. Houdre, and U. Oesterle, "Improved 60° bend transmission of submicron-width waveguides defined in two-dimensional photonic crystals," J. Lightwave Technol. **20,** 1198–1203 (2002).
10. G. P. Nordin, S. Kim, J. Cai, and J. Jiang, "Hybrid integration of conventional waveguide and photonic crystal structures," Opt. Express **10,** 1334–1341 (2002), http://www.opticsexpress.org.
11. M. Snir, S. Otto, S. Huss-Lederman, D. Walker, and J. Dongarra, *MPI—The Complete Reference* (MIT Press, Cambridge, Mass., 2000).
12. C. Guiffaut and K. Mahdjoubi, "A parallel FDTD algorithm using the MPI Library," IEEE Antennas Propag. Mag. **43,** 94–102 (2001).
13. A. Taflove and S. C. Hagness, *Computational Electrodynamics: The Finite-Difference Time-Domain Method* (Artech House, Boston, Mass., 2000).
14. K. Okamoto, *Fundamentals of Optical Waveguides* (Academic, New York, 2000).
15. http://oedcad.jlu.edu.cn.
16. E. Marcatili, "Improved coupled-mode equations for dielectric guides," IEEE J. Quantum Electron. **QE-22,** 988–993 (1986).
17. R. Syms and J. Cozens, *Optical Guided Waves and Devices* (McGraw-Hill, New York, 1992).